

Landslides (2013) 10:37–54
 DOI 10.1007/s10346-011-0310-8
 Received: 8 December 2010
 Accepted: 30 November 2011
 Published online: 24 December 2011
 © Springer-Verlag 2011

J. Travelletti · J.-P. Malet · K. Samyn · G. Grandjean · M. Jaboyedoff

Control of landslide retrogression by discontinuities: evidence by the integration of airborne- and ground-based geophysical information

Abstract The objective of this work is to present a multitechnique approach to define the geometry, the kinematics, and the failure mechanism of a retrogressive large landslide (upper part of the La Valette landslide, South French Alps) by the combination of airborne and terrestrial laser scanning data and ground-based seismic tomography data. The advantage of combining different methods is to constrain the geometrical and failure mechanism models by integrating different sources of information. Because of an important point density at the ground surface ($4.1 \text{ points m}^{-2}$), a small laser footprint (0.09 m) and an accurate three-dimensional positioning (0.07 m), airborne laser scanning data are adapted as a source of information to analyze morphological structures at the surface. Seismic tomography surveys (P-wave and S-wave velocities) may highlight the presence of low-seismic-velocity zones that characterize the presence of dense fracture networks at the subsurface. The surface displacements measured from the terrestrial laser scanning data over a period of 2 years (May 2008–May 2010) allow one to quantify the landslide activity at the direct vicinity of the identified discontinuities. An important subsidence of the crown area with an average subsidence rate of 3.07 m year^{-1} is determined. The displacement directions indicate that the retrogression is controlled structurally by the preexisting discontinuities. A conceptual structural model is proposed to explain the failure mechanism and the retrogressive evolution of the main scarp. Uphill, the crown area is affected by planar sliding included in a deeper wedge failure system constrained by two preexisting fractures. Downhill, the landslide body acts as a buttress for the upper part. Consequently, the progression of the landslide body downhill allows the development of dip-slope failures, and coherent blocks start sliding along planar discontinuities. The volume of the failed mass in the crown area is estimated at $500,000 \text{ m}^3$ with the sloping local base level method.

Keywords Slope failure · ALS data · TLS data · Seismic tomography · Discontinuity · Geological model

Introduction

A challenge to progress in landslide research is to define the geometry of the failed mass and the possible failure mechanism precisely in order to better forecast their spatial and temporal patterns of development. From a geological point of view, unstable slopes affected by landslides can be broadly divided into strong rock types and soft rock types of failure (according to the International Society for Rock Mechanics [ISRM] classification of rock and soil strength; ISRM 1981; Hoek and Bray 2004) with a transitional evolution among these two broad categories. In most strong rock slopes, preexisting discontinuities control the landscape morphology. As a consequence, unfavorable regional scale preexisting fractures are often the main predisposing factors of large landslides (Cruden 1976; Agliardi et al. 2001; Sartori et al. 2003; Hoek

and Bray 2004; Eberhardt et al. 2005; Jaboyedoff et al. 2009). In soft rock slopes (e.g., weakly cemented sedimentary units such as highly weathered and fractured rocks, conglomerates, sandstones, and clays), the heritage of preexisting structures can also play an essential role on the failure mechanisms. For example, Irfan (1998) showed that the slope behavior in saprolitic soil is controlled not only by the weathered material itself but also by relict discontinuities, particularly when these are unfavorably oriented with respect to the slope face. Undercut slopes affected by buttress removal are among the typical failure mechanisms that occur in soft rocks, leading to the development of shear zones at depth (Leroueil 2001; Cruden and Martin 2004).

In landslide investigations, a combination of several direct and indirect techniques is very often used, and several complementary ground-based and airborne-based technologies have been developed in the last decade to provide spatially distributed information about the structure. In combination with field observations and classical geotechnical investigation, the ground-based techniques are mainly two-dimensional (2D) and three-dimensional (3D) electrical resistivity and seismic tomographies (Jongmans and Garambois 2007), and the airborne-based techniques are mainly radar interferometry techniques (InSAR), Light detection and ranging techniques (LiDAR), and correlation of optical imageries (Travelletti et al. 2011; Jaboyedoff et al. 2009). Terrestrial laser scanning (TLS) and airborne laser scanning (ALS) are very efficient techniques for characterizing the morphostructure (Feng and Röshoff 2004; Slob and Hack 2004; Jaboyedoff et al. 2009) and the kinematics of landslides (Rosser et al. 2007; Monserrat and Crosetto 2008; Travelletti et al. 2008; Prokop and Panholzer 2009) because they provide a rapid collection of field topographical data with a high density of points within a range of several hundreds of meters. Possible mechanisms affecting the slope can then be estimated from the displacement vectors at the ground surface (Crosta and Agliardi 2003; Jaboyedoff et al. 2004a), such as the geometry of the slip surface (Casson et al. 2005; Travelletti et al. 2008; Oppikofer et al. 2009).

In strong rock types of failure, the morphostructures identified at the ground surface often reflect the internal geometry of the deformation (Agliardi et al. 2001; Eberhardt et al. 2005). The extensions of persistent structures in depth are more difficult to identify in soft rocks because these lithologies are very often affected by low-persistence, closely spaced joints that occur in a wide variety of orientations. The landslide kinematics in soft rocks can be both controlled by regional discontinuities and recent internal failure surface under development in the rock mass (Irfan 1998). The development of new circular or planar failures, which partly encompass the intact rock, is therefore possible as observed, for example, in weathered basalts or sandstones (Hoek and Bray 2004). Another example of weak rocks is evaporite lithology that is particularly exposed to dissolution processes. They generally form smooth

topographies at a regional scale, which make the identification of regional discontinuities difficult from morphostructure analyses at the ground surface or through digital elevation models (DEMs) (Travelletti et al. 2010). Additional surveys are, thus, necessary to complement this lack of information in depth.

In the last decade, the applications of seismic tomographies for landslide investigations showed that S- and P-wave velocities are of interest techniques to characterize properties such as the layering, the degree of fracturing, and the stiffness of the material (Grandjean et al. 2006; Jongmans et al. 2009). The internal strain affecting soft-rock landslides usually induces a velocity contrast between the unstable mass and the stable bedrock (Caris and van Asch 1991, Méric et al. 2007; Jongmans and Garambois 2007). Grandjean et al. (2006) showed that seismic velocities are much more sensitive to the degree of fracturing than the electrical resistivity tomography techniques, which complement geological and geomorphological assessments.

Still, a major difficulty consists in interpreting and integrating all the available data in a coherent framework to provide a complete picture of the landslide structure.

This work presents a multitechnique approach to characterize the structure of the upper part of the La Valette landslide (South French Alps) by combining high-resolution seismic tomographies, airborne and terrestrial LiDAR surveys (ALS, TLS), and geomorphological analyses. First, the geomorphological and historical setting of the landslide is presented; then, the methodology used to analyze the multisource data is detailed and the sloping local base level (SLBL) method is applied to estimate the landslide volume. Finally, a

kinematic model explaining the failure mechanism in the upper part of the landslide is proposed and discussed.

Geomorphological and historical features of the La Valette landslide

The La Valette landslide, originated in 1982, is one of the most important large and complex slope movements in the South French Alps. The landslide associates two styles of activity: a mudslide type of behavior with the development of a flow tongue in the medium and lower part, and a slump type of behavior with the development of several rotational and planar slides in the upper part at the main scarp. The landslide extends over a length of 2 km for a variable width of 0.2 km in the lower and medium parts, to 0.5 km in the upper part (Fig. 1a). The maximum depth, estimated by seismic and electrical resistivity tomography and geotechnical boreholes, varies from 25 m in the lower and middle parts (Evin 1992; Travelletti et al. 2009) to 35 m in the upper part (Le Mignon 2004). The mean slope gradient is ca. 30° in the scarp area and ca. 20° in the mudslide area (Fig. 1b). The volume of the landslide body is estimated at $3.5 \times 10^6 \text{ m}^3$.

The landslide affects a hillslope located uphill of the municipality of Saint-Pons (Alpes-de-Haute-Provence) and poses a significant threat for the 170 community housings located downstream (Le Mignon and Cojean 2002). The occurrence of rapid mudflows triggered from the landslide body and in the scarp area in the 1980s and 1990s conducted to the development of an early-warning system since 1991 composed of a survey network of benchmarks, optical and infrared camera monitoring and the installation of debris height detection sensors in the run-out channel, and the drainage of the lower part of the landslide.

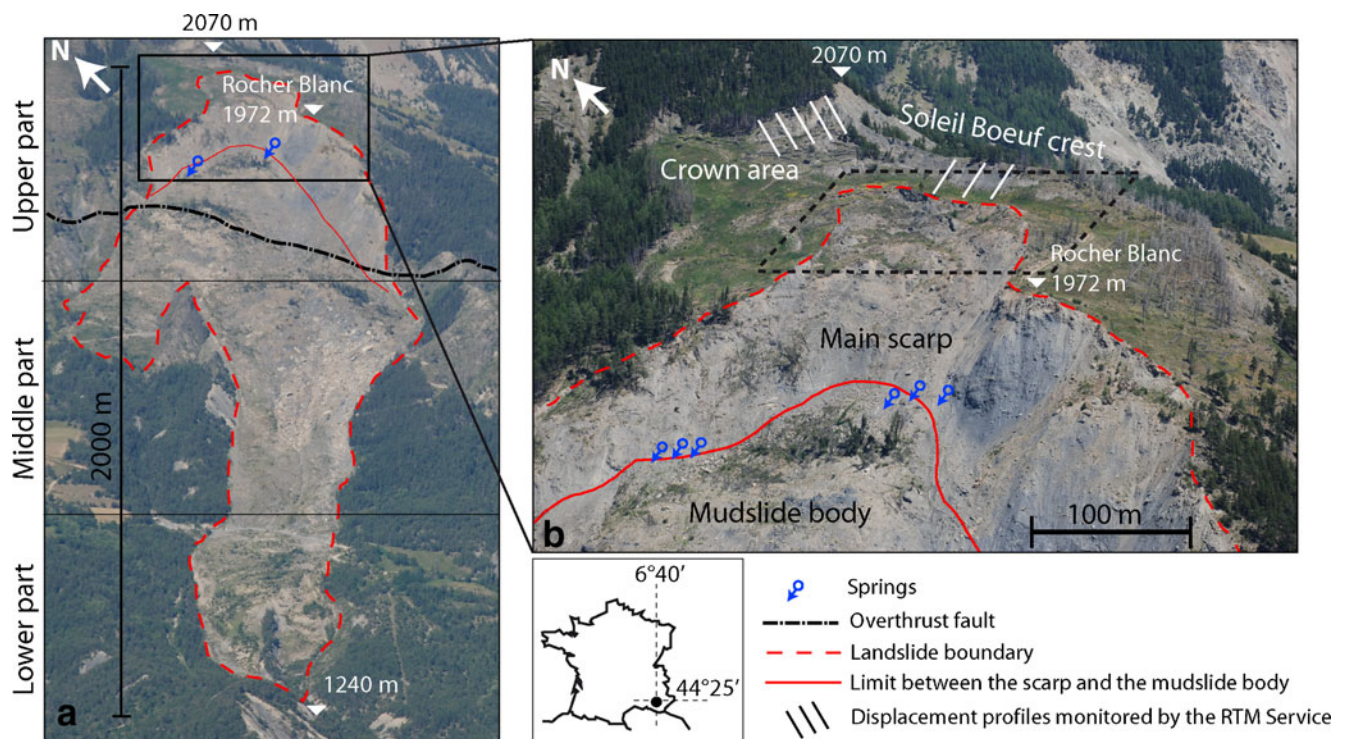


Fig. 1 Geomorphological setting of the La Valette landslide on the south-facing slope of the Barcelonnette basin. **a** General view of the landslide to the northeast. **b** View of the main scarp and the crown areas; the dashed line delineates the area investigated by TLS and seismic tomographies. The displacement profiles measured by the "Restauration des Terrains de Montagne, RTM" office to monitor the retrogression of the crown are also indicated

Geological setting

From a geological viewpoint, the La Valette landslide is located at the overthrust fault between two major lithologies outcropping in the geologic window of the Barcelonnnette basin (southeast France; Fig. 2a):

- An autochthonous formation represented by the closely stratified Callovo-Oxfordian black marls (e.g., “Terres Noires”) and characterized by a typical landscape of badlands. This formation is located in the middle and the lower parts of the slope. The bedding plane is characterized with a decametric alternance of carbonate beddings within the marls. This formation dips constantly toward 083° , with an inclination of 23° in the landslide surroundings.
- An allochthonous formation represented by two nappes and in which the upper part of the landslide has developed. The basal nappe is a tectonic wedge belonging to the Pelat Nappe and is composed of highly fractured flysch and planktonic carbonates

of the Turonian and Paleocene Superior age (BRGM 1974). This formation has a few dozen of meters of thickness at the location of the main scarp, with an average dip direction and dip of $135^\circ/30^\circ$. The Pelat Nappe is overlaid by the upper Autapie Nappe composed of highly fractured Helminthoïd flyschs, sandstones, marls, and schists. This formation is dated at the Upper Cretaceous–Upper Eocene (BRGM 1974). The tectonic discordance between the autochthonous and the allochthonous ($052^\circ/16^\circ$) materializes the major thrust fault delimiting the Barcelonnnette basin and constitutes a weak zone where many landslide source areas are located (Le Mignon 2004). Generally, the bedding plane, the fold axes, and the schistosity are very difficult to identify with certainty at the outcrop scale due to the high variability of the orientation measurements and the bad rock mass quality, which does not ensure that the rock outcrop is in place. Therefore, the geological observations of persistent structures carried out in the field indicate only the regional structural and tectonic patterns.

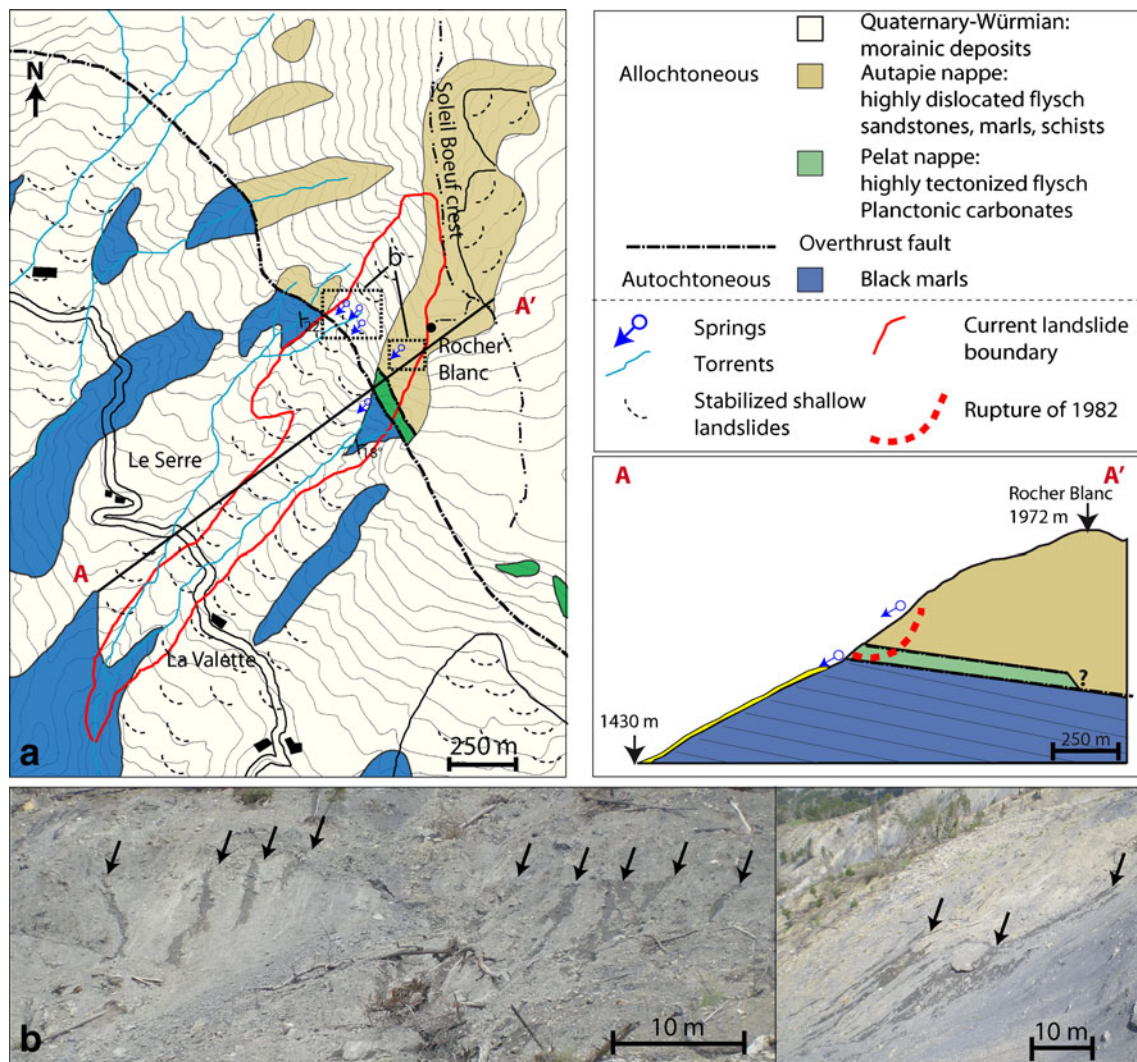


Fig. 2 Geological setting of the La Valette landslide. **a** Extract of the regional geological map at 1:50,000 with the topography before the landslide event (adapted from BRGM, 1974) and schematic cross section detailing the hydrogeological setting of the slope before the failure of 1982 (adapted from Colat and Locat, 2003). The interval between elevation contour lines is 20 m. **b** Photographs of the spring line at an elevation of ca. 1,880 m along a possible weak zone above the tectonic discordance near the northwest boundary and the Rocher Blanc location

Hydrogeological setting

From a hydrogeological viewpoint, the tectonic discordance has an important role on the landslide hydrology. Due to the high heterogeneity of the landslide material and of the highly dislocated texture of the flysch, both materials are considered as aquifers at the scale of the landslide. At the opposite, the black marls formation is considered as an aquitard (Dupont and Taluy 2000; Le Mignon 2004). Consequently, the contrast of permeability between the black marls and the flysch controls the spatial occurrence of several springs and marshy areas observed in the direct vicinity of the overthrust fault between an elevation of 1,870 and 1,950 m (Fig. 2a, b). According to Le Mignon (2004), a spring (the “Rocher Blanc” spring at 1900 m) is currently partially buried by the landslide. Consequently, a deep water circulation affects the hydrological regime of the upper part of the landslide, but the characteristics of the water flows (fluxes, quality) are unknown. Near the northwest boundary of the landslide, springs are remarkably aligned at an elevation of 1,880 m. They are likely connected to the Rocher Blanc spring through a discontinuity buried by the landslide. Remediation works were built by the local stakeholders in charge of the prevention (Service of “Restauration des Terrains de Montagne”, RTM) in order to drawdown and buffer the hydraulic heads within the landslide. Subhorizontal drains below the major overthrust fault were installed in the 1990s, but their maintenance was too difficult due to the rapid shearing of the tubes. The most efficient mitigation solution has been the installation of shallow drainage systems in the middle and lower parts of the landslide to impede streaming water to infiltrate the landslide.

Landslide historical and recent development

The landslide exhibits a complex style of activity in space and time. It has developed, first, as a rotational slide affecting the Autapie Nappe in relation to a major overthrust fault, following important rainfalls favoring fast snow melting (Colas and Locat 1993; Le Mignon 2004). The failed mass has progressively loaded the underlying black marls formation, and the landslide has developed by a series of rapid mudflows triggered in the marls such as in March 1982, April 1988, March 1989, and March 1992. The most important acceleration occurred in 1988 when a mudflow of 50,000 m³ triggered at an elevation of 1,400 m propagates over a run-out distance of ca. 500 m (Colas and Locat 1993). Up to now, these mudflows did not mobilize the complete failed mass. The displacements are monitored with topometric benchmarks since 1991 (Squarzoni et al. 2005), differential dual-frequency GPS (Déprez et al. 2010), and an extensometer since 2008, as well as at regular periods by digital correlation of satellite images (LePrince et al. 2008) and satellite radar interferometry (Squarzoni et al. 2003).

Two main aspects can be pointed out from these studies and from the observations by the local stakeholders. The first one is the decrease of velocity (from 0.4 mday⁻¹ to about 0.01 mday⁻¹) in the middle and lower parts of the landslide caused by the local groundwater drawdown since the installation of a drainage system in the 1990s. The second is the important activity since the year 2000 of the upper part at the Soleil Boeuf crest, which is characterized by a rapid retrogression of the main scarp toward the northeast and an enlargement of the landslide toward the northwest (Fig. 3). In response to this worrying situation, the RTM Service has installed several additional benchmarks along profiles both in the unstable and stable

parts of the Soleil-Boeuf crest to monitor the displacements in the crown area (Figs. 1b and 4). Actually, an accumulation of material and a steepening of the slope are observed in the upper part of the landslide because of the retrogression of the scarp. Consequently, the possible hazard scenario consists in the undrained loading of underlying black marls formation and the triggering of new rapid and mobile mudflows.

Methodology

The recent increase of activity in the crown and in the main scarp areas has motivated further investigations to define the possible volume of material still able to fail and to better understand the failure mechanisms in that part of the slope. Geological observations, small-scale morphostructural analysis with ALS data, large-scale kinematical analysis with TLS data, and a morphostructural analysis in depth with seismic tomographies have been carried out since 2008 (Figs. 1b and 4).

Geological observations of the discontinuities in the main scarp and in the crown areas

Field investigations in the scarp area are focused on the identification and the orientation of the major morphostructures and discontinuities measured with a geological compass and mapped with a differential GPS. The landslide scarp is characterized by slopes ranging from 25° to 55° over a maximum height of 80 m and a crown width of 170 m. The crown area is characterized by a complex morphology formed by a dense network of tension tracks and shear fissures in the weathered flysch formation of the Autapie Nappe forming a graben-like morphology. Counterslopes with accumulated water are also observed. The tension cracks present a subvertical dip distributed along the circular shape of the crown. This spatial distribution is typical for failures in soft rocks (Cornforth 2005). The complex morphology is cut by three main persistent discontinuities, D₁, D₂, and D₃, visible over a distance of several hundred meters (Fig. 5).

The D₁ fracture coincides with the direction of the Soleil Boeuf crest, which represents the upper boundary of the landslide. D₁ is characterized with a dip direction and a dip of 247°/42° ± 6°/4°. Because striations identified over the entire height of the crest present an orientation nearly parallel to the dip and dip direction of D₁ (calcite recrystallization, pitch of S86°), the landslide is sliding above D₁ without shearing component. The observed striations are a direct mechanical consequence of the sliding along D₁.

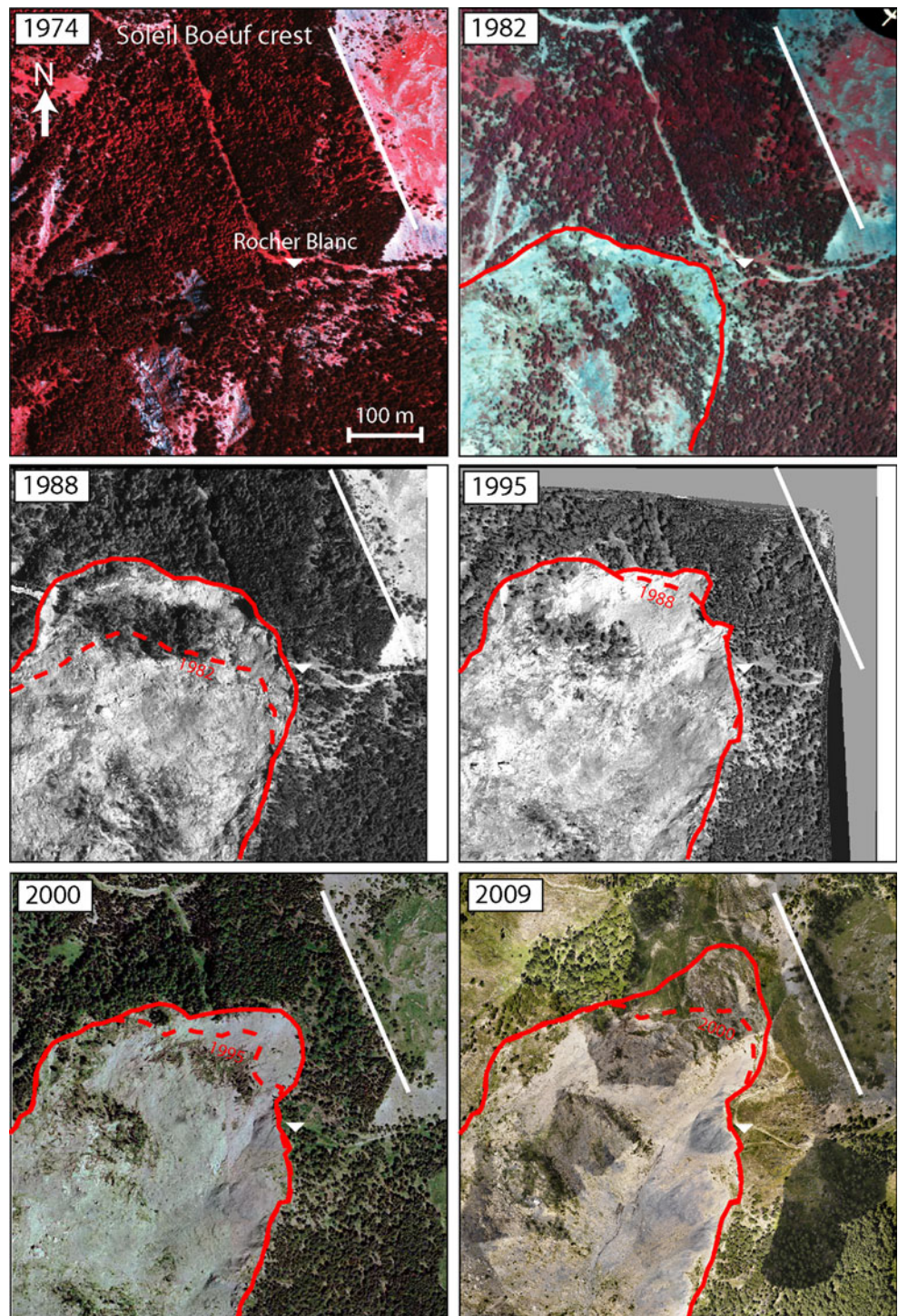
The fractures D₂ and D₃ are characterized with dip directions and dips of 287°/55° ± 4°/5° and 166°/44° ± 10°/4°, respectively. D₂ is located in the northeast of D₁, and D₃ is the conjugate fracture of D₂. The landslide is sliding along D₂ and D₃ with a shearing component. The most active part of the landslide is actually constrained between these two discontinuities.

Laser scanning surveys

Acquisition of ALS data

In order to determine the spatial extent of the main morphostructural features, regional-scale analysis of ALS has been carried out. The ALS survey was performed in July 2009 with the handheld airborne mapping system of the *Helimap* company at a constant elevation of 300 m above the ground topography,

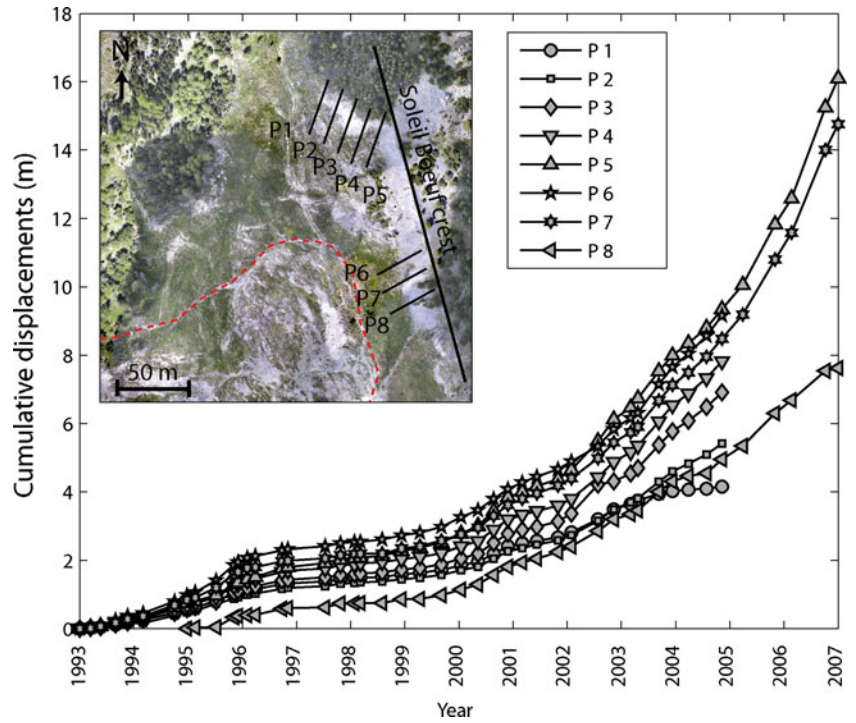
Fig. 3 Development of the La Valette scarp since 1974 (before the failure) to 2009 from the analysis of aerial orthophotograph. From 1982 to 2009, a scarp regression of 200 m toward the northeast is observed



inducing a laser footprint at the ground surface of about 0.09 m (Vallet and Skaloud 2004). The measurement device is composed of a GPS receiver (Topcon Legacy GGD with a record frequency of 5 Hz), an inertia measurement unit (a record frequency of 500 Hz) that provides the orientation of the laser beam in space and a scanner unit (Laser Riegl Q240i) configured to record last pulses of the ground surface with an acquisition frequency of 10,000 points s^{-1} . Table 1 summarizes the specification of the ALS survey. The orientation of the

system is obtained in real time, with an accuracy estimated at 0.07 m. The maximum scanner range is about 850 m, with an aperture angle of 60°. After vegetation filtering, an average point density of 4.1 points m^{-2} is obtained. A 0.5-m mesh DEM from the ground surface elevation points has been generated with a Delaunay triangulation. The DEM was then used to calculate a shaded relief map and a difference map with a 10-m mesh DEM interpolated from topographic contour lines before the landslide event (maximal elevation error, 10 m).

Fig. 4 Displacement monitoring of some profiles along the crown (monitoring carried out by the "Restauration des Terrains de Montagne, RTM" office). The monitoring indicates an acceleration of the displacement since 2000. The displacement profiles measured by RTM are also indicated on the orthophotograph of 2009



Acquisition of TLS data

Displacement monitoring of the upper part of the landslide has been carried out by repeated TLS data acquisitions. The displacement monitoring device consists of a long-range

terrestrial laser scan Optech ILRIS-3D based on the time-of-flight distance measurements using an infrared laser (Slob and Hack 2004). Mirrors inside the scanner allow the acquisition of a 40° wide and 40° high field of view in a single

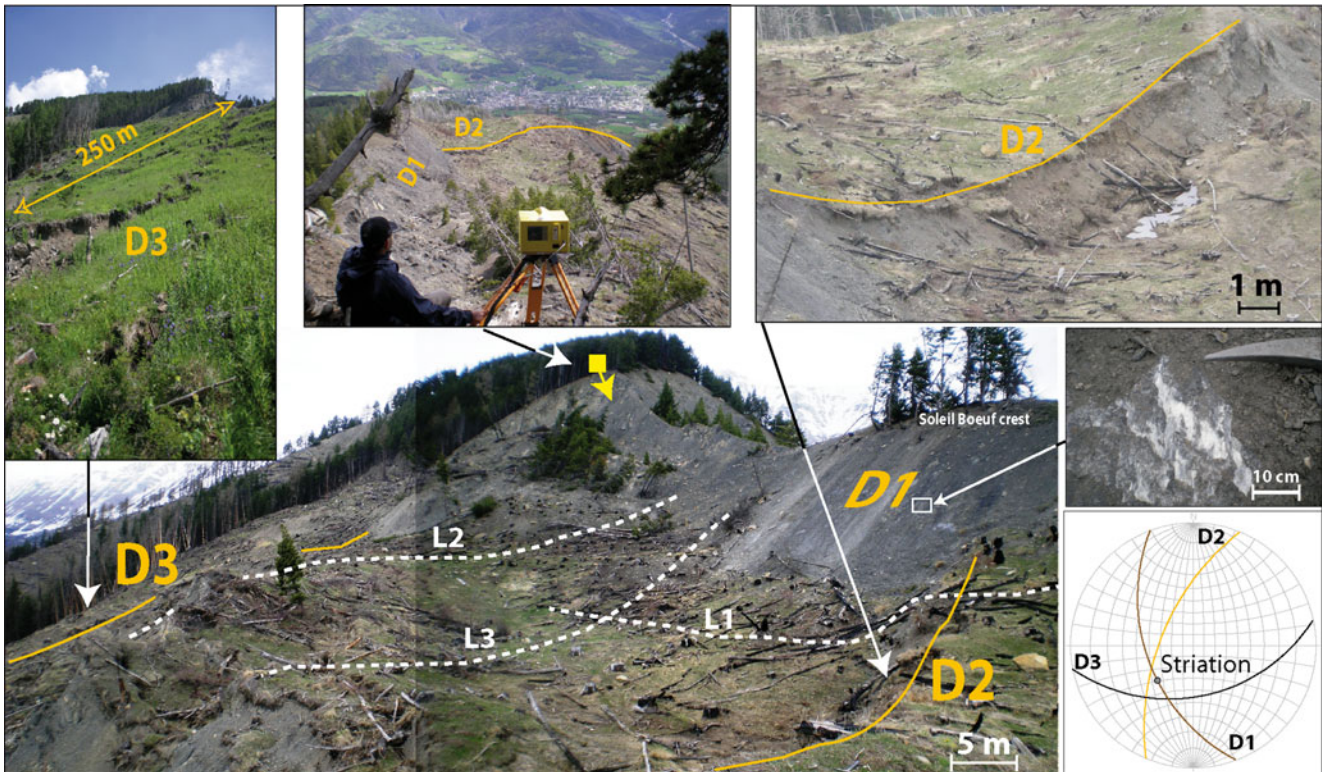


Fig. 5 Photographs of the crown area presenting three major discontinuities D1, D2, and D3 and the associated stereonet (equal angle, lower hemisphere). Striations are observed on D1. The location of the TLS (yellow square) and the seismic profiles (L1, L2, and L3) are also indicated

Table 1 Characteristics of the LiDAR data sets

Characteristics of the laser scanning systems	ALS	TLS
Scanner type	Riegl VQ480	Optech ILRIS-3D
Distance measurement technique	Time-of-flight	Time-of-flight
Wavelength (nm)	1,500	1,500
Field of view (in width and height) (°)	60	40
Laser spot diameter at 100 m (cm)	~3	~3
Frequency of measurements (Hz)	10,000	2,500
Characteristics of the field acquisitions		
Scan distance (m)	~300	~130
Pulse mode	Last echoes	Last echoes
GPS frequency (Hz)	5	Scan from a base position
Point density after vegetation filtering (points m ⁻²)		
Average	4.1	154.8
Standard deviation	4.3	140.6

acquisition with about 2,500 points s⁻¹, with an effective range up to 800 m in field conditions (Table 1).

Seven TLS data sets were acquired over the period 18 May 2008 to 27 May 2010 from the same base position (Fig. 5); the scanned area was orientated in the direction of the discontinuity D2 at a distance of 130 m from the base. At that distance, the beam width diameter is estimated at 0.03 m. The discontinuity D1 (Soleil Boeuf crest) along the main scarp was systematically included in the scanning. The TLS data sets comprise 9 to 12 million points, and the resulting mean point density on the ground surface is about 150 points m⁻² at a distance of 130 m. Only the last return pulse is registered to maximize the number of points at the ground surface.

Vegetation filtering, coregistration, and georeferencing of the sequential TLS data sets

The TLS data sets were processed and analyzed using the Polyworks v.11 software (InnovMetric 2009). The vegetation filter consists of an automatic selection of the points localized beyond a minimum height relative to a low-resolution square-grid DEM surface computed on the sequential point clouds. In this study, the mesh size of the low resolution DEM was fixed at 0.5 m and the minimum height at 0.1 m. The filtering result is systematically controlled and manually refined. A coregistration procedure is then used for aligning the sequential TLS point clouds in the same coordinate system. The coregistration applied in this study follows the methodology proposed by Teza et al. (2007) and Oppikofer et al. (2009). The sequential point clouds alignment is limited to a stable part in the image corresponding to the Soleil Boeuf crest. First, a manual alignment procedure is used; then, an automated Iterative Closest Point (ICP) algorithm is applied to minimize (least square method) the distance between the points belonging to the different sequential data sets. The coregistration procedure mainly depends on the accuracy of the ICP algorithm, which is very sensitive to the roughness of the terrain and the accuracy of the measurements (Lee et al. 1999). Rough terrains yield higher reliability in the coregistration. Therefore, a high point density was systematically acquired in this area to increase the

topographic resolution (~0.3 point cm⁻²). A good confidence is given to the coregistration quality because of the large size of the stable area of the image used for the coregistration (1,000 m²) in reference to the size of the moving area not introduced in the coregistration procedure (4,300 m²). The direct proximity of both areas in the data sets is also an advantage for an accurate coregistration.

For the absolute georeferencing, the ALS point clouds were used as a reference. The sequential TLS data sets were aligned as single-point clouds on the ALS point cloud. The coregistration accuracy of the sequential point clouds is thus not affected by the georeferencing accuracy of the ALS point cloud and is estimated at 0.07 m for the planar and vertical accuracy (Vallet and Skaloud 2004).

Accuracy of the TLS point clouds

In order to assess the accuracy associated with the TLS measurements, repetitivity measurements were realized on a planar stratum of the main scarp and corresponding to the black marls formation (9 m²). This test zone is located approximately perpendicular to the laser beam direction at a distance of 120 m from the TLS base. The average point spacing was fixed at 0.15 m. The point cloud acquisition was compared with a reference (first acquisition, May 2008) using the ICP algorithm to calculate the misfit between each pair of points in both acquisitions theoretically located at the same position. The repetitivity analysis indicates that the measurement error of the TLS used in this study follows a normal distribution characterized with an average error u of 1.0×10^{-3} m and a standard deviation σ of 1.2×10^{-2} m. This calculated error is in agreement with the range of error given by the manufacturer.

The accuracy of coregistration procedure is given by the residual 3D misfit computed on the stable part of the TLS of the 18 May 2008 taken as the reference (Table 2). The same procedure is applied to assess the error of the absolute positioning relative to the ALS survey. The higher error in the absolute positioning is mainly related to the lower point density and accuracy of the ALS data sets, providing less geomorphological details than the TLS survey (Table 2).

Table 2 Average error μ and standard deviation σ of the relative and absolute coregistration of the TLS data sets

	Relative positioning error		Absolute positioning error	
	μ (m)	σ (m)	μ (m)	σ (m)
18 May 2008	–	–	0.04	0.07
25 July 2008	0.00	0.03	0.06	0.08
10 May 2009	0.00	0.03	0.02	0.07
12 July 2009	0.00	0.02	0.04	0.09
8 October 2009	0.00	0.03	0.00	0.07
26 April 2010	0.00	0.02	0.01	0.07
27 May 2010	0.00	0.03	0.01	0.07

Displacement characterization and quantification

The displacements are calculated by comparing the TLS data sets with the reference. Two methods are used to quantify the displacements from the original point clouds. The first method is based on the shortest distance (SD) comparison of point clouds. The second uses displacements of specific points (SPs).

The SD comparison consists of computing for each point the distance to its nearest neighbor in the reference point cloud. This method is particularly useful to detect spatially distributed changes if the direction of movement is unknown and to define zones with different displacement directions (Oppikofer et al. 2009). In order to determine the vertical displacement affecting the upper part of the landslide, the SD is constrained to compute displacement only along the vertical direction (SDv), assuming a tolerance angle for the vertical direction of $\pm 10^\circ$. The results are therefore comparable with elevation changes computed

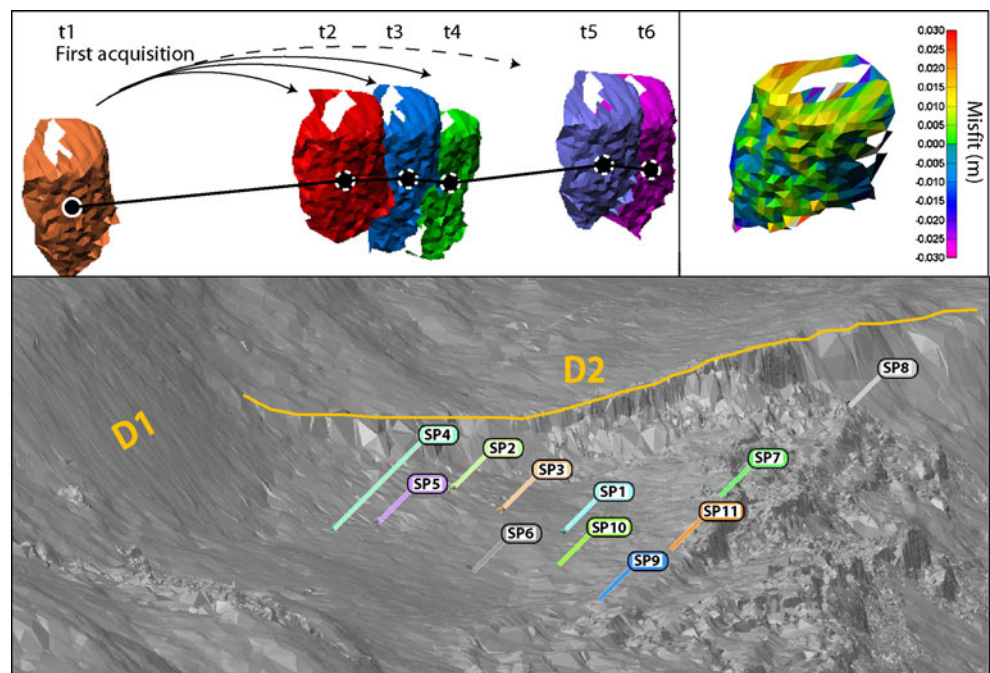
with differential DEMs (Bitelli et al. 2004). The accuracy of the vertical displacement depends on two independent factors: (1) the coregistration accuracy and (2) the computed distance D according to the tolerance angle, which gives a maximal error $E_{max}(E_{max} = D * \sin(10^\circ))$.

The observed movement of SPs allows one to define the direction of displacements. In this study, natural SPs were chosen (Fig. 6). They consist of tree stumps recognizable in the unfiltered sequential point clouds. In order to assess the displacements of the SPs in the crown area, a method based on the roto-translation technique is used (Monserrat and Crosetto 2008; Oppikofer et al. 2009). It takes into account both translation and rotation of individual objects and uses the very high density available in the point clouds. Eleven SPs were triangulated in the plane normal to the laser viewing direction in order to minimize the effect of shadow zones in the interpolation (Fig. 6). To calculate the true displacement field, the center points of the SPs in the first acquisition are determined by averaging the X , Y , Z positions of the points forming the SPs. Then, the triangulated SPs of the reference are aligned on their corresponding triangulated SPs in the sequential point clouds using the ICP algorithm implemented in Polyworks (Fig. 6). Finally, the displacement vectors of the SPs are given by the initial and final positions of the center points of the first acquisition. Because the SPs are very well defined, the error mainly depends on the coregistration accuracy of the sequential point clouds.

Seismic tomography investigation

Because the laser scanning data provide only information on the structure and the kinematics visible at the ground surface, additional geophysical data to obtain information in depth were acquired in order to better constrain the interpretation. Seismic tomography has proven to be an efficient technique to detect the

Fig. 6 Location of the 11 SPs in the crown area used to calculate the displacements. The SPs of the first acquisition are aligned on their corresponding displaced SPs for each acquisition date. The displacement of the center point of each SP of the first acquisition is used to determine the displacement vector. The average misfit between the SP of the first acquisition and the corresponding SP is estimated at ca. 0.01 m



contact between a landslide body (highly fractured) and a stable bedrock in the same type of geological setting as for La Valette (Jongmans et al. 2009, Grandjean et al. 2006; Grandjean et al. 2007). Three seismic tomography surveys of P- and S-wave velocities (L1, L2, L3) have been carried out in the upper part of the landslide to characterize the seismic velocities (V_p , V_s) of the failed material and determine the extension in depth of the discontinuities D1 and D2 (Fig. 5). Two cross sections were installed along the direction of the main slope, and one cross section was installed perpendicular to the previous line in order to cross the discontinuity D2.

The two longest devices are composed of 24 geophones (resonance frequency, 10 Hz) spaced 5 m each in order to obtain a sufficient investigation depth for a large-scale characterization of the landslide structure. The shortest devices, composed of 24 geophones spaced 2 m each, bring information on the fracturing between the failed material and the bedrock. For the seismic source, 100 g of pentrite was used for each shot. The processing of the first arrival travel time P wave was carried out with the Rayfract seismic tomography software based on the wavepath Eikonal traveltimes inversion algorithm (Schuster and Quintus-Bosz 1993). Figure 7a shows an example of the arrivals of the P waves and surface waves. Dispersion of surface waves is closely related to the structure and properties of the landslide material and, in particular, to shear wave velocity. The vertical distribution of the shear wave velocity can be estimated on the basis of the dispersion analysis of different kinds of surface waves contained in the P-wave seismic records (Fig. 7b). The dispersion analysis results in the generation of a dispersion curve (frequency vs. phase

velocity) for each geophone location. The shear waves velocity sections were, therefore, obtained using a spectral analysis of the surface waves method with the surf96-CPS program (Hermann 1987), which allows one to analyze the dispersive character of surface waves (McMechan and Yedlin 1981) and to obtain a S-wave vertical velocity profile by one-dimensional (1D) inversion of the dispersion curves (Tarantola 2005) (Fig. 7b). To derive a 2D section, the 1D shear-wave velocities inverted from each local dispersion curve are then interpolated along each seismic line.

In order to georeference the 2D tomographies, the location of each geophones was measured with a dGPS (horizontal and vertical accuracy values of 0.04 and 0.07 m). In each profile, the geophone locations are then projected on a straight line in the local coordinate system calculated with a linear regression. The equations of the regression line allow one to allocate a 3D position in the local coordinate system for all nodes of the tomography.

Estimation of the volume of the failed mass

To estimate the volume of the failed mass, the SLBL method has been used. It is a generalization of the base level concept proposed by Mills (2003) and is defined as a surface above which the rocks are assumed to be erodible by landslides due to the absence of buttress (Golts and Rosenthal 1993; Jaboyedoff et al. 2004b). This method was successfully applied both on hard and soft rock slopes (Jaboyedoff et al. 2009; Travelletti et al. 2010). The SLBL method is used in this study by integrating the information from the seismic survey and the TLS interpretation.

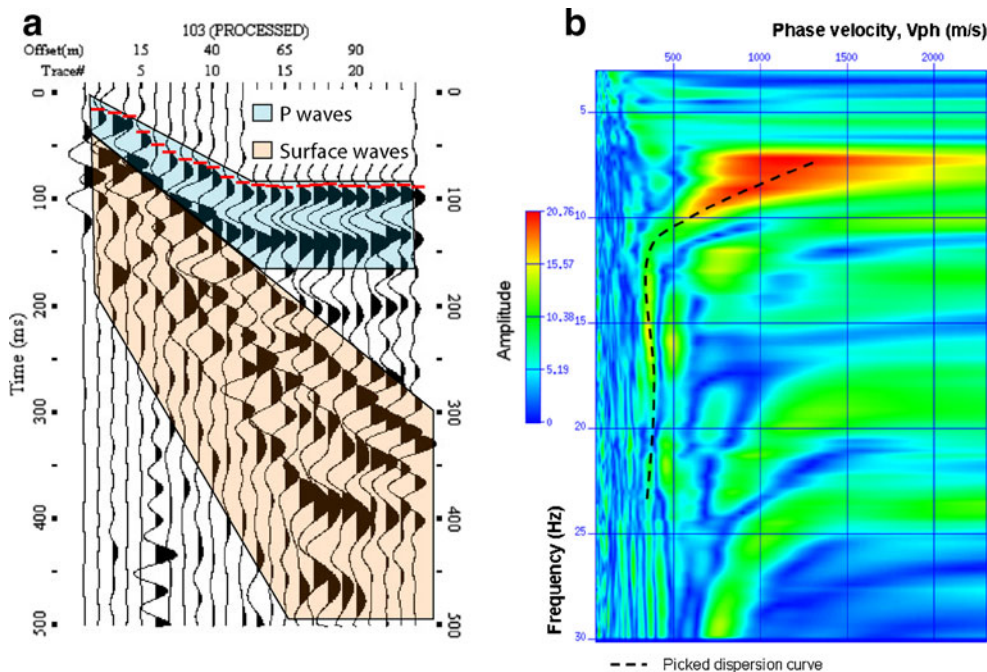


Fig. 7 Example of seismic tomography data from the profile L2 (see location in Fig. 5). **a** Example of recordings of the P-wave and surface-wave arrival time. The first arrivals of the P waves are used for the inversion of the P-wave velocity tomography. A spectral analysis of the surface waves is realized to measure the surface wave dispersion curve and invert the corresponding shear wave velocity. **b** Example of the analysis of the dispersive character of surface waves for the 1D inversion of a vertical profile of shear wave velocity. The phase velocity represents the velocity of individual wave propagation in the media according to its wavelength and frequency (Park et al. 1998). The relative good determination of the dispersion curve (dashed line) gives confidence on the inverted shear-wave velocity profile

The SLBL algorithm is based on an iterative routine that replaces the elevations of any mobile point of a DEM by the mean value of the altitude of its neighbors, allowing a certain tolerance. Points with an altitude (z_i) larger than the mean of their neighbors are replaced by the mean value of the two neighbors $(z_{i-1} + z_{i+1})/2$ or by this value plus a tolerance C . Explicitly, in 2D, the procedure can be formalized as follows (Jaboyedoff et al. 2004b):

$$\text{If } z_i > (z_{i-1} + z_{i+1})/2, \text{ then } z_i = (z_{i-1} + z_{i+1})/2 \quad (1)$$

The result is a straight line between z_{i-1} and z_{i+1} . The introduction of the tolerance value C leads to a second-degree curve:

$$\text{If } z_i > (z_{i-1} + z_{i+1})/2 - C, \text{ then } z_i = (z_{i-1} + z_{i+1})/2 \pm C \quad (2)$$

The tolerance can produce holes between points, for example, with an altitude smaller than the altitude of the surroundings points. To avoid this, two additional conditions can be added to ensure that the new point has a higher altitude than the lowest of its neighbors:

$$\begin{aligned} \text{If } z_i > (z_{i-1} + z_{i+1})/2 - C \text{ and} \\ (z_{i-1} + z_{i+1})/2 \pm C > z_{i-1} \text{ or} \\ (z_{i-1} + z_{i+1})/2 \pm C > z_{i+1}, \text{ then} \\ z_i = (z_{i-1} + z_{i+1})/2 \pm C \end{aligned} \quad (3)$$

If it is not the case, the altitude z_i of the point i is replaced by the lower altitude of its neighbors. The procedure is iterative and is stopped once the change between two iterations is near a zero value, and a failure surface nearly circular is obtained if the tolerance used is very different from zero. In order to take into account planar sliding along discontinuities, a small tolerance has to be used to fit the calculated failure surface on the observed discontinuities. In 3D, the procedure is similar, but the test is then performed using the highest and lowest values among the four closest neighbors. Some points must be fixed during the computation to avoid the calculation of a flat topography. The discontinuities determined in this study from the field observations, the seismic tomographies, and the TLS surveys are used to constrain the SLBL computations.

Results

Morphostructural analysis

The combined analysis of the geological field observations, the shaded relief map, and the differential DEM map allows one to propose a kinematic model of the landslide retrogression.

Although the highly dislocated flysch formation can be considered as a relatively soft rock, the shaded relief analysis with the differential DEM clearly demonstrates that, at regional scale, the key factor controlling the failure geometry and the overall stability of the mass is not the flysch formation itself but the spacing and the orientation of the discontinuities composed by D1, D2, and D3.

Consequently, the upper part of the La Valette landslide can be divided in four terrain units (Fig. 8a).

Since the triggering date in March 1982, the terrain unit 1 has been confined between the steep discontinuities D2 and D3 that constrained the landslide retrogression to the northeast. The failed mass is composed of coherent blocks (up to 50 m wide), which are sliding toward the main slope direction. These blocks form minor counterslopes affected by multiple open tension cracks (up to 1 m in opening and in spacing) favoring water infiltration. The blocks are progressively dislocated and incorporated in the mudslide body downhill. The negative elevation difference developing along D1 indicates that the landslide retrogression to the northeast is limited by D1, which forces the retrogression to develop laterally to the north (Fig. 8b). As a consequence of the loss of buttress given by the terrain unit 1, the terrain units 2 and 3 are progressively destabilized. The terrain unit 4 (northwest side of D3) is characterized with a hummocky morphology indicating a lower destabilization of the slope due to the loss of buttress provided by the terrain unit 3 located downhill.

At a regional scale, the La Valette landslide appears to be included in a Deep-Seated Gravitational Slope Deformation (DSGSD) (Agliardi et al. 2001), in which main scarp coincides with the extension of D1 to the north. In addition, the Soleil Boeuf crest presents the same morphology as before the triggering in 1982 when the scarp was located 200 m more to the southwest (Le Mignon 2004). Therefore, the 1982 large failure is strongly suspected to be a reactivation of an older DSGSD along D1. Furthermore, the dip-and-dip direction of the western side of the DSGSD main scarp ($166^\circ/38^\circ \pm 10^\circ/4^\circ$) is very similar to D3, suggesting that the old scarp face belongs to the same discontinuity set. Consequently, D3 can thus be a preexisting fracture that is also reactivated. The difference in the fracturing degree on both sides of D2 clearly highlights the preferential extension of the landslide toward the northwest. On the southeast side of D2, no significant geomorphic evidence of current activity is observed except the extension of D1, which progressively disappears in the flysch formation to the southeast. Furthermore, no negative elevation difference is noticed in this area in reference to the vertical accuracy of the differential DEM (~10 m).

The downhill limit of the negative elevation remarkably coincides with the tectonic discordance of the Autapie Nappe, and the uphill limit corresponds to the spring area. The location of the triggering area of 1982 is clearly identified where the elevation difference (50 m) is the maximum.

Seismic tomography analysis

The tomographies of P and S waves reveal a low-velocity zone ($V_p < 900 \text{ ms}^{-1}$, $V_s < 400 \text{ ms}^{-1}$) in the terrain unit 1 affected by dense fracturing. The increase in P- and S-wave velocities when one gets closer to the stable rock (fracture D1) gives a good confidence in the determination of the contact among the failed mass and the stable bedrock in depth (Fig. 9a, b). The velocities in the stable part composed of the flysch formation vary in the range 1,200–2,000 m s^{-1} for the P waves and 450–600 m s^{-1} for the S waves. These velocity values are slightly lower than those expected for similar rocks composed of conglomerate and sandstone with a low clay content (Gosar et al. 2001). They are explained by the highly dislocated texture of the flysch (BRGM 1974). Despite an important velocity contrast in Vs on both sides of D2, the extension of D2 in depth cannot be precisely

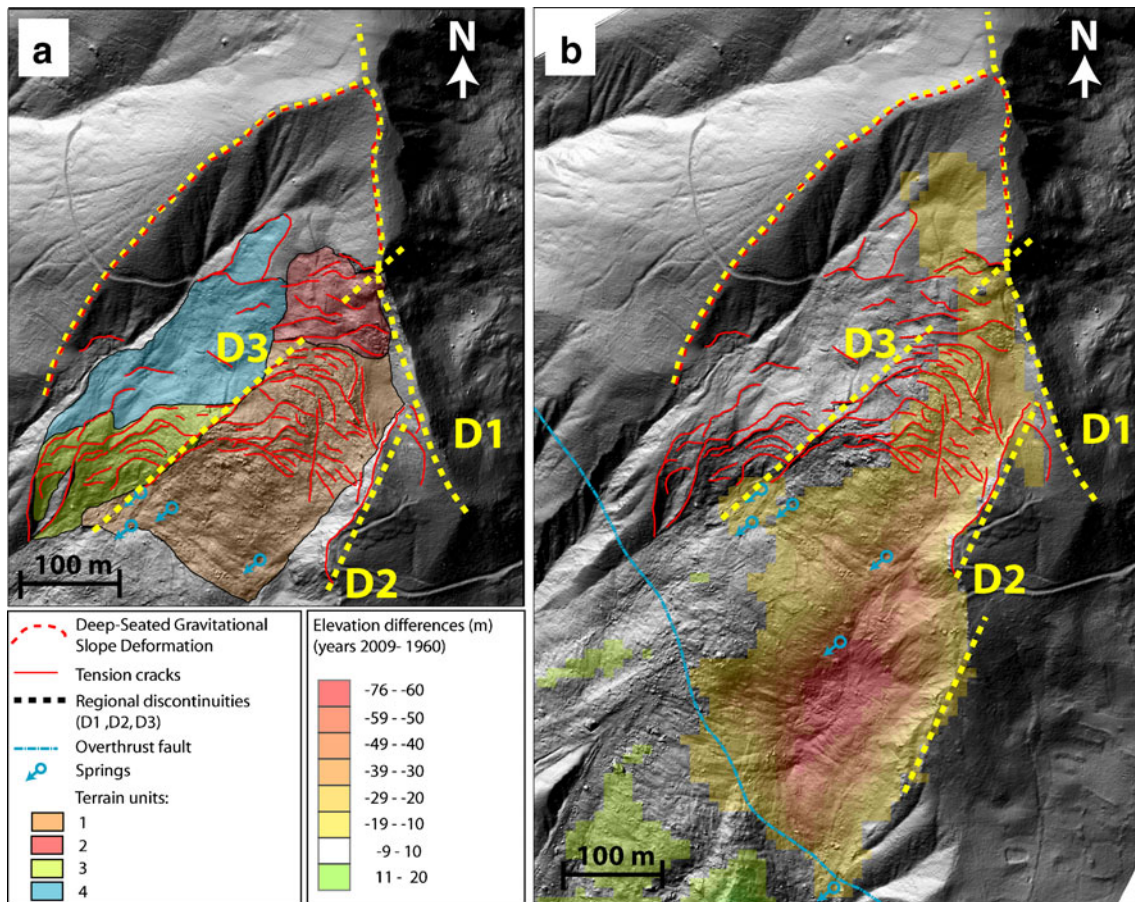


Fig. 8 Morphostructural maps derived from the interpretation of an ALS survey. **a** Major discontinuities and subunits identified in the scarp and in the crown areas. **b** Differential DEM highlighting the retrogression direction of the landslide for the period 1960–2009 constrained by the discontinuity D2 and D3

determined on the tomographies because of insufficient velocity contrast in depth. Starting from the stable part, the iso-values of $1,200 \text{ ms}^{-1}$ (V_p) and 450 ms^{-1} (V_s) dip rapidly below the ground surface. This interface can be followed in all seismic tomographies between 12 and 15 m below the ground surface. It is difficult to determine the roughness of this interface knowing that the seismic tomographies very often tend to produce artificial undulating surfaces because of the diffractions caused by small irregularities at the shallow surface of very heterogeneous media.

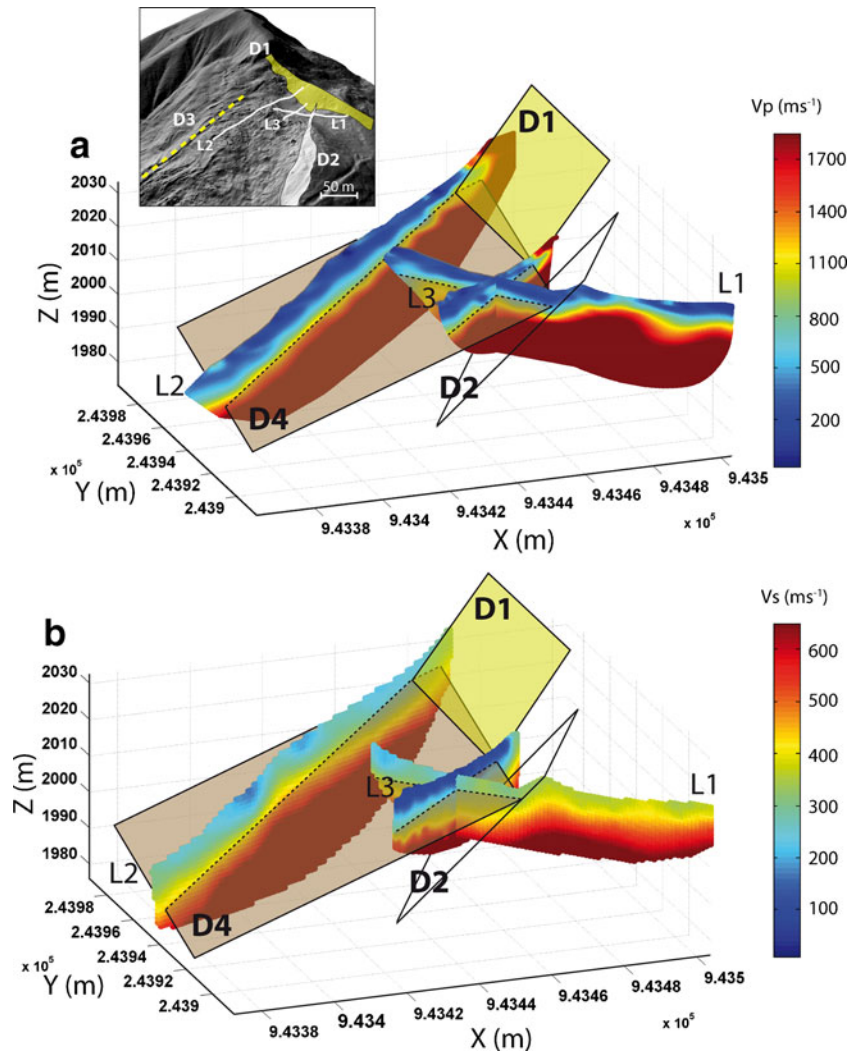
Therefore, the interface can be modeled as a plane, which is an acceptable assumption for a regional-scale interpretation. The plane is adjusted in a least square sense on the tomography nodes at the transition between the velocities characterizing the failed mass and the stable bedrock, respectively. A stronger weight is attributed to the V_p tomographies because the velocity contrasts are more important than in the V_s tomographies. The accuracy is estimated by adjusting different planes based on five different interpretations. The average orientation is, thus, characterized with a dip direction of $233^\circ \pm 8^\circ$ and a dip of $26^\circ \pm 4^\circ$, which is close to the average slope of the ground surface but lower than D1. Therefore, this interface is not interpreted as the extension of D1 in depth but as the limit of D4 between a highly fractured media and the less fractured bedrock in flysch. D4 could possibly correspond to an internal shear zone upon which a highly fractured rock is sliding in a dip-slope configuration.

Kinematics analysis

Displacements calculated from the TLS data sets between the periods May 2008 and May 2010 illustrate the landslide activity at the vicinity of D1, D2, and D3. The SDv computations on the point clouds indicate a maximum absolute elevation difference of 6.14 m between July 2008 and May 2010 (average error of $3 \times 10^{-3} \text{ m}$ with a standard deviation of 0.03 m), leading to a maximum vertical displacement rate of 3.07 m year^{-1} along D1 and D2 of the top of the terrain unit 1 (Fig. 10). All the displacements in the terrain unit 1 are concentrated between D1 and D2 where tensions cracks are developing, thus explaining the low seismic velocities observed in this area (Fig. 9).

The elevation differences allow one to distinguish three coherent blocks 1a, 1b, and 1c belonging in the terrain unit 1 (Fig. 8a); these blocks are progressively separated by the opening of tension cracks and the sliding along D1 and D2. Uphill, the terrain unit 2 is also destabilized due to the loss of buttress provided by terrain unit 1. No displacement is detected on the southeast side of D2 with reference to the accuracy of the TLS data sets (less than 0.05 m). These observations are in agreement with the morphostructural analysis described previously. The displacement amplitudes of the SPs are far larger than the accuracy of the TLS data sets, thus giving a good confidence in the measurements. The SP displacements allow one to determine the true 3D displacement vectors characterized by an average velocity of about 4.12 m year^{-1} (Fig. 11).

Fig. 9 3D view of the seismic tomographies with their location in the crown area. **a** P-wave velocity tomography. **b** S-wave velocity tomography. A velocity contrast at about 12 m deep highlights the presence of the discontinuity D4 interpreted as an internal sliding surface



The increase of the standard deviation of SPs displacements with the elapsed days between TLS acquisitions (Table 3) highlights the spatial heterogeneity of displacement in the top of the terrain unit 1 due to the progressive opening of tension cracks separating the blocks 1a, 1b, and 1c (Fig. 10). On the opposite, the directions of the displacement vectors are constant in time and in space, with an average dip direction and dip of $228^{\circ}/34^{\circ}$ ($\pm 4^{\circ}/\pm 2^{\circ}$) (Fig. 12). Consequently, the short-term kinematics of the terrain unit 1 seems to be mainly controlled by planar failures along D1 and D4.

Concept for the failure mechanism

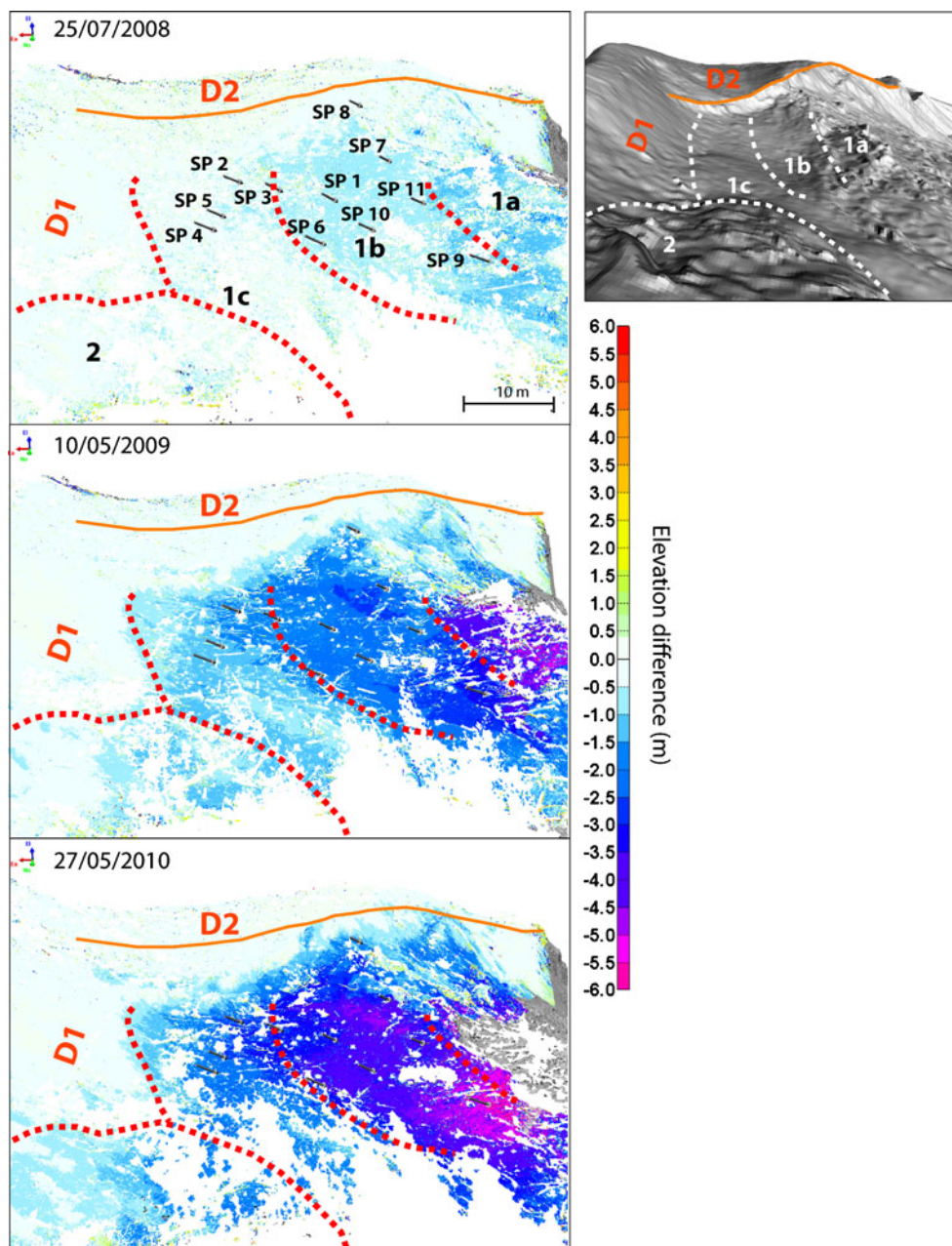
Because the upper part of the La Valette landslide is structurally controlled at regional scale by planar sliding and wedge fracture configurations, a synthesis of the structural and kinematics analysis is done by the use of horizontal hemispherical projections (equal angle) (Richards et al. 1978; Hoek and Bray 2004) (Fig. 12). The fracture sets identified in the terrain units 1, 2, and 4 are summarized in Table 4. Figure 13a presents the conceptual model of the failure mechanism interpreted from the integration of the ALS, TLS, and seismic survey.

From a kinematical point of view, D3 and D2 define a wedge geometry with an axis direction and dip of $215^{\circ}/30^{\circ} \pm 11^{\circ}/5^{\circ}$ and a

maximum depth varying between 60 and 80 m with a back-crack represented by D1. Because the wedge axis does not “daylight” in the slope face, this geometry is precluded from a strict straightforward wedge kinematic evaluation as a single homogeneous block (Hoek and Bray 2004). In other words, the wedge cannot move without a buttress breakout. Therefore, the wedge geometry can only constrain the landslide retrogression direction between D2 and D3 to the north. However, a breakout interface cannot be totally excluded at the bottom of the scarp to explain the location of the source line and the subsidence along D1 in the terrain unit 1 (Fig. 13a).

Downhill, the mudslide body is acting as a buttress for the upper part. Consequently, the progression of the mudslide allows the development of dip-slope failures, and coherent blocks start sliding along D4 laterally delimited by D2 and D3. Because the dip direction and dip of the 2-year displacements vectors in the terrain unit 1 are located between the great circles of D1 and D4 (Fig. 12), the displacement vector components are likely related to a sliding along D1 and D4, thus leading to a biplanar superimposed failure mechanism. In addition, the dip direction and dip of the displacements vectors are remarkably close to the intersection of the great circles of D2 and D3, which corresponds to the wedge axis

Fig. 10 TLS point cloud comparisons according to the reference date of 18 May 2008. The displacements are calculated with the SD comparison in the vertical direction. A negative value means that the point elevation is lower than the point of the reference. Several blocks are clearly individualized through time. The blocks 1a, 1b, and 1c belong to the subunit 1. The block 2 belongs to the subunit 2. The displacement vectors of the SPs are also indicated



orientation (Fig. 12). This observation consolidates the hypothesis of the predominant role of the wedge geometry on the long-term development of the landslide since its triggering date, while the planar sliding explains the short-term landslide kinematics. D4 is probably not a preexisting discontinuity and is likely related to a plastic deformation of the highly fractured flysch formation during the development of the dip-slope failure mechanism. The tension cracks observed at the ground surface are certainly connected to the shear zone D4 in depth, thus leading to a listric geometry, which is usually observed in soft rocks and clay slopes.

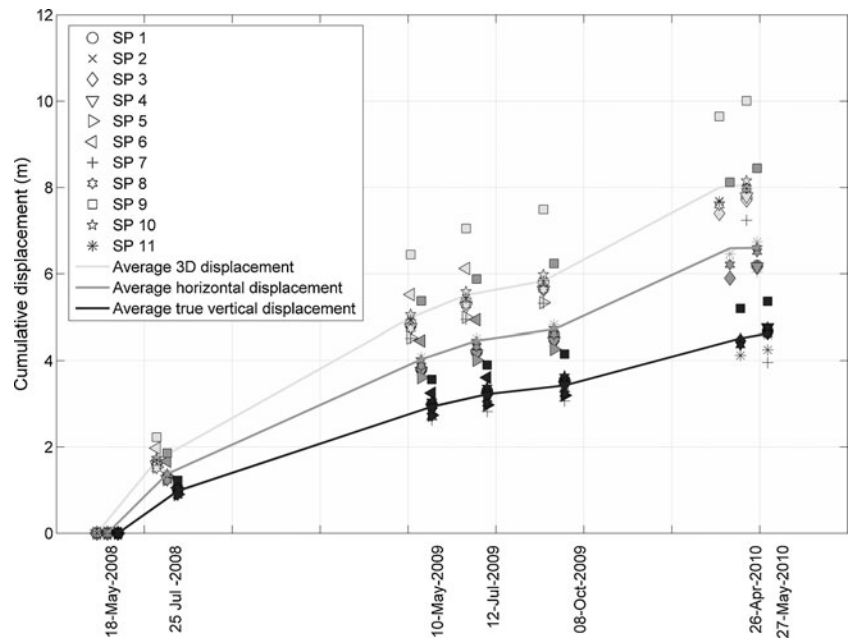
Volume estimation with the SLBL method

To estimate the volume of the failed mass along D4 in the terrain unit 1, an interpolation is carried out using the SLBL method. The discontinuities D1 (northeast limit), D2 (southeast limit), D3

(northwest limit), and D4 (basal limit in depth) are used to constrain the calculation domain of the SLBL by assuming that D4 is continuous with a slightly curved geometry. The mechanical weak zone highlighted by the spring line at the lower limit of terrain unit 1 (Figs. 8 and 13a) is used as the southern limit for the SLBL calculation. The unstable volume is calculated using a 2-m grid DEM interpolated from the ALS data. This cell size is essentially used for computation stability and time-computing purposes. A tolerance of -0.3 defining the degree of curvature of the SLBL is selected in such way that the SLBL surface fits at best the discontinuity D4.

The result gives a slightly curved surface that flattens and daylight in the spring line. A volume of $500,000 \text{ m}^3$ is estimated (Fig. 13b). This volume represents the highly fractured mass mobilized by D4, which is currently loading the underlying mudslide body.

Fig. 11 Cumulated displacements of the SPs calculated with the roto-translation technique



Discussion and conclusion

In the La Valette landslide, the morphostructural analysis and the displacement analysis indicated a structurally controlled evolution of the landslide at a regional scale. The retrogression failure observed in the upper part of the La Valette landslide is an intermediate case study between landslide developed in soft and in strong rocks. In strong rocks, the relationship between preexisting fractures and the failure mechanism has been widely observed and illustrated (Sauchyn et al. 1998; Agliardi et al. 2001; Jaboyedoff et al. 2009). In soft rocks, the failure mechanism is propagated through intact materials of uniform shear strength (Irfan 1998). Therefore, conventional stability analyses are not fully appropriate because of the influence of both the mechanics of the discontinuities and the mechanics of the deforming soil. Although this aspect is out of the scope of this study, it will need specific attention for a further slope failure modeling. In addition, in such slow-moving complex landslides in soft rocks, it is often difficult to determine the exact location of the failure surface. The deformation may occur at more than one level or in different parts of the slope at different times (Cornforth 2005). Therefore,

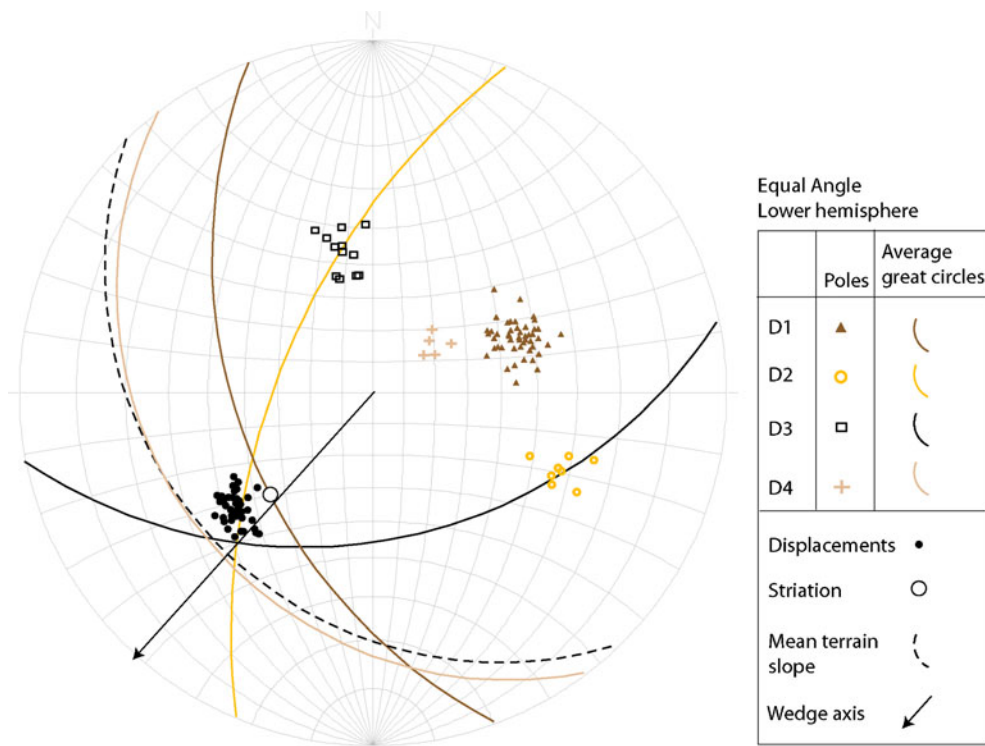
several additional failure surfaces not depicted in the conceptual model may be present in reality or may occur in the future. However, the proposed model is coherent with the ALS, TLS, and seismic data and the field observations.

The upper part of the La Valette landslide is very probably a case of reactivation of an older landslide and is characterized with a succession of individual slides, as it is often observed in a large DSGSD (Agliardi et al. 2001). A first slide occurs, and as a consequence of the movement of this mass, other adjacent masses starts to move, thus allowing the retrogression of the landslide to the north. The opening of tension cracks in the crown area is evidence of the initiation of a progressive failure. However, the flysch formation may already have undergone some deformation before the discontinuities start to open. The failure may have started in the weak zone D4 and along the preexisting fractures D1, D2, and D3. Furthermore, the prefailure behavior of successive slides is probably a consequence of nonuniform stress and strain conditions, which prevent the upper part to a catastrophic failure. In the same way, the dip of D4 extended by the SLBL calculation (internal sliding surface mobilizing 500,000 m³ of the landslide mass) is very close to the residual friction angle of the reworked flysch (30°) (Colas and Locat 1993; Le Mignon 2004; Fig. 13b). Therefore, the stability limit is not reached simultaneously in the whole mass, and it would be very unlikely that the unstable mass will fail in a single event. Because the wedge axis delimited by D2 and D3 does not daylight in the slope face, the probability of a catastrophic failure is considerably reduced to a progressive release of material through shallow translational failure mechanisms controlled by D1 and D4. However, the existence of breakout interfaces at the bottom of the main scarp cannot be totally excluded (Fig. 13a). Stresses would then be transferred by loading to the mudslide body acting as a reinforced buttress

Table 3 Average μ and standard deviation σ of the SPs displacements

	Elapsed days	μ (m)	σ (m)
18 May 2008–25 July 2008	68	1.69	0.07
25 July 2008–10 May 2009	289	3.3	0.34
10 May 2009–12 July 2009	63	0.52	0.05
12 July 2009–08 Oct. 2009	88	0.39	0.09
08 October 2009–26 April 2010	200	1.93	0.17
26 April 2010–27 May 2010	31	0.34	0.05

Fig. 12 Stereonet (equal angle, lower hemisphere) of the major discontinuities observed in the scarp and in the crown areas. The direction of displacement located between the great circles of D4 and D1 near the intersection of D2 and D3 strongly suggests that the upper part of the La Valette landslide is structurally controlled by planar failure confined within a wedge geometry



since the setup of the drainage system in the middle part of the slope and the decrease of the mudslide velocity. The stress release occurs over an extended period due to the continuous sliding of the mudslide body ($\sim 1 \text{ m year}^{-1}$). However, this buttress can become overstressed if the activity of the upper part increases, thus potentially leading to a sudden acceleration of the mudslide or the development of an upper internal failure in the mudslide body. If the stress increment becomes excessive, the amount of deformation becomes deviated in the shallow part of the slope, thus leading to an increase of the slope inclination favoring shallow failures. Sudden releases of small volumes and fluidization of the mass at the vicinity of the spring line have been observed in the past and more recently in spring 2009 when about $3,000 \text{ m}^3$ of reworked flysch suddenly mobilized in a mudflow over a distance of 250 m. A development of the mudslide in areas where the buttress is less strong typically in the borders of the mudslide through lateral spreading is also possible. As a consequence of the important activity of the upper part, the lower mudslide part has to evolve differently than in the past according to the

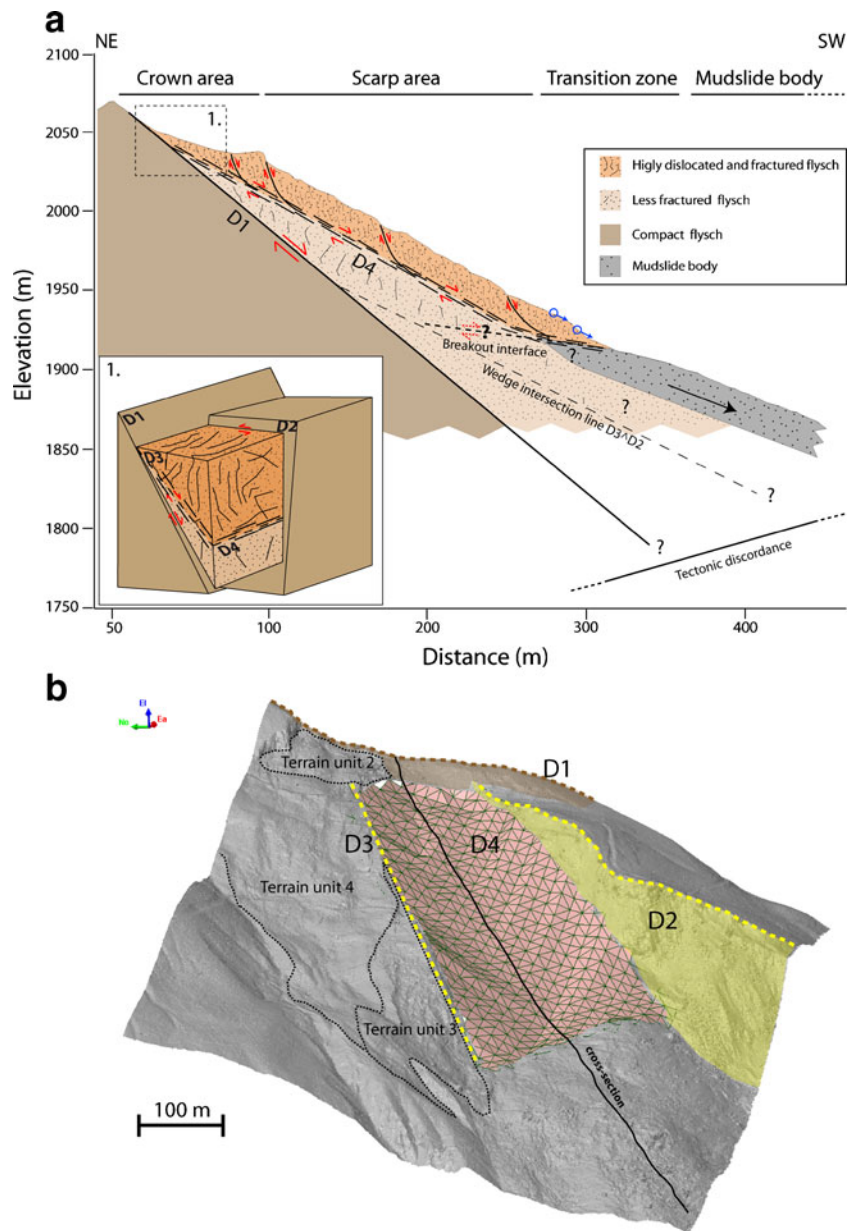
drainage works installed further downhill. The transition between the main scarp and the mudslide body constitutes a key zone controlling the overall landslide behavior because that part is susceptible to be overstressed. Groundwater conditions of the upper part still need to be assessed in detail for a better understanding of the failure mechanisms. Hydromechanical modeling in progress will also help to better understand the failure mechanism.

To conclude, the efficiency of combining ground-based (LiDAR TLS, seismic tomography) and airborne-based (LiDAR ALS) geophysical information to characterize the landslide structure is demonstrated by the agreement observed between geological field observations, morphostructural modeling, and kinematics analysis. The advantage of combining different methods is to propose an interpretation adapted to the scale of the landslide, which is not possible when only local (e.g., punctual) measurements are used. TLS data provide high-resolution point clouds of the topography for large-scale analysis, which complements ALS data that are more suitable for regional-scale analysis. The seismic tomography survey provides spatially distributed information on the geometry of the fractures in depth. The integration and the interpretation of this multi-source data allow one to propose possible landslide evolution scenarios. Furthermore, this study demonstrated that in soft rocks (e.g., flysch formations), the morphostructure information derived from field observations and DEMs analysis do not fully reflect the internal structure of the slope without complementary information on the kinematics and on the internal structure provided with ground-based surveys. The proposed multitechnique approach can be applied to different types of landslides. A simple plot of the

Table 4 Characteristics of the fracture sets identified in the terrain units 1, 2, and 4 of the La Valette landslide

	Number of observations	Dip direction (°)	Dip (°)
D1	52	247	42
D2	11	287	55
D3	77	166	44
D4	5	233	26

Fig. 13 Conceptual geological model of the development of the upper part of the La Valette landslide. **a** Proposed concept of the failure mechanism affecting the scarp and the crown areas. The morphostructural and the kinematics analyses highlight a planar failure mechanism along D1 and D4 confined in a wedge geometry delimited by D2 and D3. The location of the cross section is shown in image b. **b** 3D view of the discontinuity D4 extended with the SLBL computation. The ground topography above D4 has been removed



displacement vector in a stereonet with the observed discontinuity orientations can highlight structurally controlled landslides. This approach has been illustrated in the monitoring of strong rock slope. Because multisource data have heterogeneous qualities and different spatial resolutions, a major difficulty consists in the extraction of relevant information and in their integration in a coherent framework. Data georeferencing and reinterpretation are among the most important steps needed to detect inconsistencies among multisource data (Caumon et al. 2009; Travelletti and Malet 2011). A future challenge to improve the proposed methodology relies on coupling of 3D Geographic Information Systems (data storage and management) with 3D geometrical modeling packages, allowing quick reinterpretation of the conceptual model of the slope.

Acknowledgements

This work was supported by the European Commission under the Marie Curie Contract “Mountain risks: from prediction to management and governance” (FP6, MCRTN-035798; 2007–2010) and by the French Ministry of Research within the project “SISCA: Système Intégré de Surveillance de Crises de glissements de terrain argileux” (Contract ANR Risk-Nat, 2009–2012). The authors would like to acknowledge Mr. Georges Guiter and Mr. Michel Peyron from *Restauration des Terrains en Montagne* (Office of Barcelonnette) for their assistance and discussion in the field. The authors are also grateful to Mr. Grzegorz Skupinski (University of Strasbourg) for his support in the acquisition of the TLS data. The authors are also grateful to two anonymous reviewers for their constructive comments.

References

- Agliardi F, Crosta G, Zanchi A (2001) Structural constraints on deep-seated slope deformation kinematics. *Eng Geol* 59:83–102
- Bitelli G, Dubbini M, Zanutta A (2004) Terrestrial laser scanning and digital photogrammetry techniques to monitor landslide bodies. In: Proceedings of the XXth ISPRS Congress 'Geo-Imagery Bridging Continents', XXXV, Part B5, Istanbul, Turkey, 12–23 July 2004, ISPRS, pp 246–251
- Caris JPT, van Asch ThWJ (1991) Geophysical, geotechnical and hydrological investigations of a small landslide in the French Alps. *Eng Geol* 31(3–4):249–276
- Casson B, Delacourt C, Allemand P (2005) Contribution of multi-temporal sensing images to characterize landslide slip surface—application to the La Clapière landslide (France). *Nat Hazard Earth Syst Sci* 5:425–437
- Caumon G, Collon-Drouaillet P, Carlier L, de Veslud C, Sausse J, Visuer S (2009) Teacher's aide: 3D modeling of geological structures. *Math Geosci* 41(9):927–945
- Colas G, Locat J (1993) Glissement et coulée de La Valette dans les Alpes-de-Haute-Provence. Présentation générale et modélisation de la coulée. *Bulletin de Liaison des Laboratoires des Ponts et Chaussées* 187:19–28
- Cornforth DH (2005) *Landslides in practice: investigation, analysis and remedial/preventative options in soils*. Wiley, USA, 625
- Crosta GB, Agliardi F (2003) Failure forecast for large rock slides by surface displacement measurements. *Can Geotech J* 40:176–191
- Cruden DM (1976) Major slides in the Rockies. *Can Geotech J* 13:8–20
- Cruden DM, Martin CD (2004) Before the Frank Slide: preparatory & triggering causes from maps and photographs. In: Proceedings of the 57th Canadian Geotechnical Conference, GeoQuébec 2004
- Déprez A, Malet J-P, Masson F, Ulrich P (2010) (submitted) Continuous monitoring and near-real time processing of GPS observations for landslide analysis: a methodological framework. *Engineering Geology*, (submitted)
- Dupont M, Taluy P (2000) Hydrogéologie du glissement de La Valette (avec carte au 1:50000 des venues d'eau). Internal Report, Université de Savoie, Chambéry, France, p 45 http://eost.u-strasbg.fr/omiv/Publications_la_valette.html
- Eberhardt E, Thuro K, Luginbuehl M (2005) Slope instability mechanisms in dipping interbedded conglomerates and weathered marls—the 1999 Ruffi landslide, Switzerland. *Eng Geol* 77:35–56
- Evin M (1992) Prospection sismique en partie basse de la coulée de La Valette. Internal Report, RTM—restauration des Terrains en Montagne, Barcelonnette, France http://eost.u-strasbg.fr/omiv/Publications_la_valette.html
- Feng QH, Röshoff K (2004) In-situ mapping and documentation of rock faces using a full-coverage 3-D laser scanning technique. *Int J Rock Mech Min Sci* 41:139–144
- Golts S, Rosenthal E (1993) A morphotectonic map of the northern Arava in Israel derived from isobase lines. *Geomorphology* 7:305–315
- Gosar A, Stopar R, Car M, Mucciarelli M (2001) The earthquake on 12 April 1998 in the Krn mountains (Slovenia): ground-motion amplification study using microtremors and modelling based on geophysical data. *J Appl Geophys* 47:153–167
- Grandjean G, Penetier C, Bitri A, Méric O, Malet JP (2006) Caractérisation de la structure interne et de l'état hydrique de glissements argilo-marneux par tomographie géophysique: l'exemple du glissement-coulée de Super-Sauze. *Comptes Rendus Géosciences* 338(9):587–595
- Grandjean G, Malet J-P, Bitri A, Méric O (2007) Geophysical data fusion by fuzzy logic for imaging the mechanical behaviour of mudslides. *Bull Soc Géol Fr* 178(2):127–136
- Hermann RB (1987) *Computer programs in seismology*. Saint-Louis University, Saint-Louis, MO, USA, 317
- Hoek E, Bray JW (2004) *Rock slope engineering*. Civil and mining, Fourth Edition. Institute of Mining and Metallurgy, London, UK, p 456
- InnovMetric (2009) *PolyWorks User's manual—3-D scanner and 3-D digitizer software from InnovMetric Software Inc.*, <http://www.innovmetric.com/>
- International Society for Rock Mechanics (ISRM) (1981) *Rock characterization, testing and monitoring; ISRM Suggested Method*. Pergamon Press, Oxford, UK
- Irfan TY (1998) Structurally controlled landslides in saprolitic soils in Hong Kong. *J Geotech Geol Eng* 16:215–238
- Jaboyedoff M, Ornstein P, Rouiller JD (2004a) Design of a geodetic database and associated tools for monitoring rock-slope movements: the example of the top of Randa rockfall scar. *Nat Hazard Earth Syst Sci* 4:187–196
- Jaboyedoff M, Baillifard F, Couture R, Locat J, Locat P (2004b) New insight of geomorphology and landslide prone area detection using DEM. In: Lacerda WA, Ehrlich M, Fontoura AB, Sayo A (eds) *Landslides evaluation and stabilization*. Balkema, Rotterdam, pp 199–205
- Jaboyedoff M, Couture R, Locat P (2009) Structural analysis of Turtle Mountain (Alberta) using digital elevation model: toward a progressive failure. *Geomorphology* 103:6–16
- Jongmans D, Garambois S (2007) Geophysical investigation of landslides: a review. *Bull Soc Géol Fr* 178(2):101–112
- Jongmans D, Bièvre G, Renalier F, Schwartz S, Bearez N, Orengo Y (2009) Geophysical investigation of a large landslide in glaciolacustrine clays in the Trièves area (French Alps). *Eng Geol* 109:45–56
- Le Mignon G (2004) *Analyse de scénarios de mouvements de versants de type glissement-coulées. Application à la région de Barcelonnette (Alpes-de-Haute-Provence, France)*. PhD Thesis, Ecole Nationale des Ponts et Chaussées, Paris, France, p 210
- Le Mignon G, Cojean R (2002) Rôle de l'eau dans la remobilisation de glissements-coulées (Barcelonnette, France). In: Wagner P, Rybar J, Stemberk J (eds) *Proceedings of the first European Conference on Landslides*. Czech Republic, Prague, pp 239–244
- Lee BU, Kim CM, Park RH, Nurre JH, Corner BR (1999) Error sensitivity of rotation angles in the ICP algorithm. *SPIE Proc Ser A* 3640:146–156
- LePrince S, Berthier E, Ayoub F, Delacourt C, Avouac J-P (2008) Monitoring earth surface dynamics with Optical Imagery. *Eos* 89:1–5
- Leroueil S (2001) Natural slopes and cuts: movement and failure mechanisms. *Geotechnique* 51:197–243
- McMechan GA, Yedlin MJ (1981) Analysis of dispersive waves by wave field transformation. *Geophysics* 46:869–874
- Méric O, Garambois S, Cadet H, Malet JP, Guéguen P, Jongmans D (2007) Seismic noise based methods for soil landslide characterization. *Bull Soc Géol Fr* 178(2):137–148
- Mills HH (2003) Inferring erosional resistance of bedrock units in the East Tennessee mountains from digital elevation data. *Geomorphology* 55:263–281
- BRGM (Bureau des Recherches Géologiques et Minières) (1974) *Carte et notice géologique de Barcelonnette au 1:50.000*. XXXV-39. Orléans, France, p 38
- Monserrat O, Crosetto M (2008) Deformation measurement using terrestrial laser scanning data and least squares 3-D surface matching. *ISPRS J Photogramm* 63:142–154
- Oppikofer T, Jaboyedoff M, Blikra LH, Derron MH, Metzger R (2009) Characterization and monitoring of the Aknes rockslide using terrestrial laser scanning. *Nat Hazards Earth Syst Sci* 9:1003–1019
- Prokoc A, Panholzer H (2009) Assessing the capability of terrestrial laser scanning for monitoring slow moving landslides. *Nat Hazard Earth Syst Sci* 9:1921–1928
- Richards LR, Leg GMM, Whittle RA (1978) Appraisal of stability conditions in rock slopes. In: Bell FG (ed) *Foundation engineering in difficult ground*. Newnes-Butterworths, London, pp 449–512
- Rosser NJ, Petley DN, Dunning SA, Lim M, Ball S (2007) The surface expression of strain accumulation in failing rock masses. In: Eberhardt E, Stead D, Morrison T (eds) *Rock mechanics: meeting Society's challenges and demands*. Proceedings of the 1st Canada–U.S. Rock Mechanics Symposium, Vancouver, Canada, 27–31 May 2007, Taylor & Francis, pp. 113–120
- Sartori M, Baillifard F, Jaboyedoff M, Rouiller JD (2003) Kinematic of the 1991 Randa rockfall (Valais, Switzerland). *Nat Hazard Earth Syst Sci* 3:423–433
- Sauchyn DJ, Cruden DM, Hu HQ (1998) Structural control of the morphometry of open rock basins, Kananaskis region, southwestern Alberta. *Geomorphology* 22:313–324
- Schuster GT, Quintus-Bosz A (1993) Wavepath eikonal travelttime inversion: theory. *Geophysics* 58:1314–1337
- Slob S, Hack R (2004) 3D Terrestrial Laser Scanning as a new field measurements and monitoring technique. In: Hack R, Azzam R, Charlier R (eds) *Engineering geology for infrastructure planning in Europe. A European perspective*. Lecture Note in Earth Sciences. Springer, Berlin-Heidelberg, pp 179–190
- Squarzone C, Delacourt C, Allemand P (2003) Nine years of spatial and temporal evolution of the La Valette landslide observed by SAR interferometry. *Eng Geol* 68:53–66
- Squarzone C, Delacourt C, Allemand P (2005) Differential single-frequency GPS monitoring of the La Valette landslide (French Alps). *Eng Geol* 79:215–229
- Tarantola A (2005) Inverse problem theory and methods for model parameter estimation. *SIAM—Society for Industrial and Applied Mathematics*, Philadelphia, U.S.A, p 342
- Teza G, Galgano A, Zaltron N, Genevois R (2007) Terrestrial laser scanner to detect landslide displacement fields: a new approach. *Int J Remote Sens* 28:3425–3446
- Travelletti J, Malet J-P (2011) Characterization of the 3D geometry of flow-like landslides: a methodology based on the integration of heterogeneous multi-source data. *Eng Geol*. doi:10.1016/j.enggeo.2011.05.003
- Travelletti J, Oppikofer T, Delacourt C, Malet J-P, Jaboyedoff M (2008) Monitoring landslides displacements during a controlled rain experiment using a long-range terrestrial laser scanning (TLS). In: ISPRS—The International Archives of the

- Photogrammetry, Remote Sensing and Spatial Information Sciences. Vol. XXXVII. Part B5, pp. 485–490
- Travelletti J, Malet J-P, Hibert C, Grandjean G (2009) Integration of geomorphological, geophysical and geotechnical data to define the 3D morpho-structure of the La Valette mudslide (Ubaye Valley, French Alps). In: Malet J-P, Remaitre A, Boogard T (eds) Proceedings of the International Conference on Landslide Processes: from geomorphologic mapping to dynamic modelling, Strasbourg, CERG Editions, pp 203-208
- Travelletti J, Demand J, Jaboyedoff M, Marillier F (2010) Mass movement characterization using a reflection and refraction seismic survey with the sloping local base level concept. *Geomorphology* 116:1–10
- Travelletti J, Delacourt C, Allemand P, Malet J-P, Schmittbuhl J, Toussaint R, Bastard M (2011) (submitted) Correlation of multi-temporal ground-based images for landslide monitoring: application, potential and limitations. *ISPRS Journal of Photogrammetry and Remote Sensing* (submitted).
- Vallet J, Skaloud J (2004) Development and experiences with a fully-digital handheld mapping system operated from a helicopter. In: The International Archives of the Photogrammetry, Remote Sensing and Spatial Information Sciences, Istanbul, Vol. XXXV, Part B5
- J. Travelletti** (✉) · **J.-P. Malet**
Institut de Physique du Globe de Strasbourg, CNRS UMR 7516,
University of Strasbourg (EOST),
5 rue René Descartes, 67084 Strasbourg Cedex, France
e-mail: julien.travelletti@unistra.fr
- J. Travelletti**
GEOPHEN-LETG, CNRS UMR 6554,
University of Caen Basse-Normandie,
Caen Cedex, France
- K. Samyn · G. Grandjean**
Bureau des Recherches Géologiques et Minières (BRGM),
3 Avenue Guillemin, Orléans, France
- M. Jaboyedoff**
Institute of Geomatics and Analysis of Risk (IGAR),
University of Lausanne,
Lausanne, Switzerland